Zinc-Substituted Cobalt Phosphate [$ZnCo_2(PO_4)_2$] as a Bifunctional Electrocatalyst

Deepa Singh, Shashwat Singh, Ponnappa Kechanda Prasanna, Rajeev Kumar Rai, Prae Chirawatkul, Sudip Chakraborty, Maximilian Fichtner, and Prabeer Barpanda*

ABSTRACT: Development of highly efficient, earth-abundant, and stable bifunctional electrocatalysts is pivotal for designing viable next-generation metal−air batteries. Cobalt-based phosphates provide a treasure house to design electrocatalysts, with a wide range of cation substitutions to further enhance their electrocatalytic activity. In particular, phosphates with distorted geometry show favorable binding efficiency toward water molecules with low overpotential. In the present work, zinc-substituted cobalt phosphate $ZnCo_2(PO_4)_2$ was investigated. Its crystal structure was solved to a monoclinic framework built with CoO_6 octahedra and distorted CoO_5/ZnO_5 trigonal bipyramid leading to efficient bifunctional electrocatalytic activity. It offers robust structural stability with onset potential values of 0.87 V (vs reversible hydrogen electrode (RHE)) and 1.50 V (vs RHE) for oxygen reduction reaction (ORR) and oxygen evolution reaction (OER) processes, respectively, comparable to the precious metal catalysts. The origin and stability of the bifunctional activity were probed by combining ex situ diffraction and electron microscopy corroborated by *ab initio* calculations. Overall, zinc-substituted cobalt phosphate [$ZnCo_2(PO_4)_2$] forms a potential bifunctional electrocatalyst with tunable local cobalt coordination that can be harnessed for metal−air batteries.

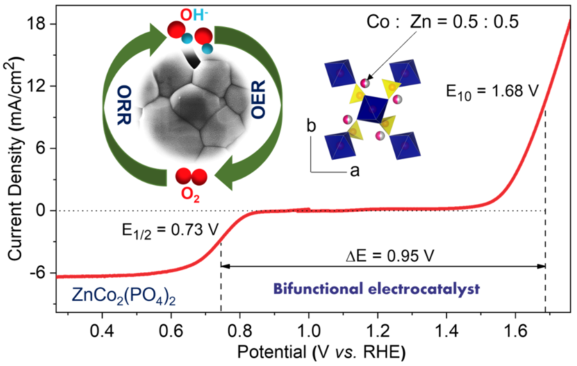

1. INTRODUCTION

The unprecedented demand for energy, growing from milliwatt to terawatt challenge, has triggered significant interest to design sustainable energy storage and conversion devices. At this point, devices like metal−air batteries and fuel cells are pursued as viable contenders due to their high energy density and conversion efficiency vis-à-vis classical insertion reaction-based batteries.[1−4] Oxygen electrochemistry is central to the functioning of metal−air batteries involving two vital electrochemical reactions, viz. the oxygen reduction reaction (ORR) and the oxygen evolution reaction (OER).[5,6] The oxygen molecules can be electrochemically reduced by taking electrons from the current collector and amalgamate with the dissolved metal in the electrolyte during discharge. A complete reverse process can occur during the charging step (OER). However, the kinetics of ORR and OER steps can be sluggish and compel the application of catalysts that can work in various aqueous electrolytes using air as the source of oxygen.[7] In particular, cleaving the very strong dioxygen bond impedes the kinetics of the oxygen reduction reaction step.[8] Hence, it presents an intimidating task to design earth-abundant, low-cost, and efficient bifunctional electrocatalysts with minimum overpotential suitable for efficient metal−air batteries.[9−11] Well-known catalysts (e.g., Pt, IrO_2, and RuO_2) containing less-abundant precious metals are expensive and selective, and thereby have restricted large-scale application.[12] However, many transition metal-based oxides/non-oxides,[13] metal−organic frameworks (MOFs), and several other systems[14] have been developed to catalyze the oxygen electrochemistry (ORR and OER) reaction in alkaline media. Manthiram et al.[15] and Shao-Horn et al.[16] showed $LiCoO_2$ and a few battery materials exhibiting good bifunctional activity in 0.1 M KOH. The OER activity of these oxides can be improved by carefully tuning their crystal structure and chemical composition. Additionally, many three-dimensional polyanionic framework cathodes have been discovered with formidable electrocatalytic performance. Among them, phosphate (PO_4)-based materials offer scalable synthesis, stable structure, chemical and thermal stability, and excellent bifunctional electrocatalytic activity.[17−19] Specifically, the Co- and Ni-based materials exhibit efficient ORR and OER activities, respectively. As per the literature, nanostructured cobalt−phosphate particles coated with nitrogen-doped carbon layers ($Co_3(PO_4)_2$@NC) can offer superior OER activity when compared to the precious metal-based IrO_2 catalyst.[20] In the case of $Mn_3(PO_4)_2$, the OER activity can be improved owing to the presence of a phosphate framework capable of stabilizing Mn^{3+} sites unlike the oxide frameworks.[21] Kang et al. demonstrated excellent OER activity in sodium cobalt pyrophosphate ($Na_2CoP_2O_7$) stemming from the distorted building blocks of cobalt tetrahedra (CoO_4).[22] Recently, our group has shown sodium cobalt (meta)phosphates as Co-containing economic bifunctional electrocatalysts.[23] Lee et al. explained the understanding of the catalytic origin of OER in the case of nickel phosphate.[24] The electrocatalytic performance of various phosphate-based frameworks can be improved by (i) unique atomic structure and local environment of the M−O bond, (ii) bending/stretching of tetrahedral (MO_4)/trigonal bipyramidal (MO_5)/octahedral (MO_6) building units, and (iii) exposed planar facets.

Encouraged by the reports on cation substitution as a way to enhance the catalytic performance in spinels,[25−27] we tried to alter the physicochemical properties of cobalt phosphates by substitution of divalent cations. This divalent cation substitution can be ideally realized by metal ions having comparable size to Co^{2+}, which can substitute into the Co site leading to distorted CoO_6 octahedra moieties without completely disrupting the crystal structure. In this pursuit, we explored the electrocatalytic performance of zinc-substituted cobalt (pyro)phosphate prepared by a solution combustion route.[28] The incorporation of larger Zn^{2+} ions (0.74 pm) into the Co sites (Co^{2+} ions ∼0.65 pm) can change the lattice parameters[29] (shown in Figure S1) and thereby oxygen affinity associated with the Co-redox centers. It can lead to improved electrocatalytic activity. For the first time, zinc-substituted cobalt phosphate [$ZnCo_2(PO_4)_2$] was found to offer stable bifunctional electrocatalytic performance in alkaline media, making it suitable for potential use in Zn−air batteries.

Moreover, it is also important to note that $ZnCo_2(PO_4)_2$ and $Co_3(PO_4)_2$ are isostructural, having a monoclinic (s.g. $P2_1/n$) structure. Both materials are isomorphous to the parent compound "γ-$Zn_3(PO_4)_2$" and with the mineral farringtonite (Mg, Fe, Mn, Ca)$_3(PO_4)_2$. The general formula can be written as γ-$(Zn_{1-z}M_z)_3(PO_4)_2$ [$0 \leq z \leq 0.50$]. Based on that, other compositions such as $Zn_2Co(PO_4)_2$ and $(Zn_{0.5}Co_{0.5})_3(PO_4)_2$ were also characterized.[30]

The detailed crystal structure of $ZnCo_2(PO_4)_2$ was solved. Involving various experimental analyses along with the density functional theory (DFT) study, we have examined the role of crystal structure, constituent transition metals, and atomic surface planes on the electrocatalytic bifunctional activity and the underlying mechanism. Eventually, the operational stability (and reversibility) of the $ZnCo_2(PO_4)_2$ electrocatalyst was assessed by several post-mortem investigations including X-ray diffraction and transmission electron microscopy techniques.

2. EXPERIMENTAL SECTION

2.1. Materials Synthesis. Zinc-substituted cobalt phosphate $ZnCo_2(PO_4)_2$ (ZCP) was synthesized by a simple solution combustion synthesis using stochiometric amounts of zinc nitrate hexahydrate ($Zn(NO_3)_2{\cdot}6H_2O$, Sigma, 99.99%) and cobalt nitrate hexahydrate ($Co(NO_3)_2{\cdot}6H_2O$, Sigma, 98%) as oxidizers, and ammonium dihydrogen phosphate ($NH_4H_2PO_4$, Sigma, 97%) as a phosphate source. All of these precursors were mixed to form a uniform solution, which was allowed to undergo a gel formation with addition of citric acid ($C_6H_8O_7$, Sigma, 99.5%) as a fuel (oxidizer/fuel; 1:1.75 molar ratio) at 150 °C with constant magnetic stirring. Later, the temperature was increased to 200 °C to onset an exothermic combustion to yield a brownish combustion ash as an intermediate product. Further, the combustion ash was calcined at 800 °C for 6 h under a steady Ar flow to obtain the target ZCP phase. The inert atmosphere aided in forming a conductive coating of amorphous carbon over pristine particles, generated from the extra fuel. Since cobalt phosphates are generally poor electronic conductors,[31] incorporating *in situ* carbon coating from the surplus fuel could boost the conductivity and electron transfer competence.

2.2. Structural Characterization. The structure of the pristine ZCP material was investigated with synchrotron X-ray diffraction (SXRD) at BL1.1W (λ = 1.03319 Å), Siam Photon Laboratory, Synchrotron Light Research Institute (SLRI), Thailand (X-ray energy of 12 keV), in reflection geometry using an array of Mythen strip detectors. The incident angle was set to 10° during the measurement, and the detector was moved to cover up to 65 or 106° Cu Kα equivalence. The exposure time was 1800 s. SXRD confirmed the primary monoclinic phase of ZCP. Further, Rietveld analysis was performed using GSAS-II with the EXPGUI front end for the acquired data.[32] The crystal structure was illustrated using VESTA software.[33] The morphologies of the pristine sample were observed by combining scanning electron microscopy (SEM; Ultra 55 FESEM Carl Zeiss EDS, operated at 5 kV) and (scanning)-transmission electron microscopy ((S)-TEM; FEI Titan Themis, operated at 300 kV).

2.3. Magnetic Susceptibility Analysis. The sample was prepared by filling 48.8 mg of ZCP material in a magnetic hydrogel capsule with some tissue paper on top and bottom to fill the remaining gaps. Then, this capsule was placed in the center of the straw, which was sealed from its ends, and the straw was placed in a magnetometer. Further, magnetic susceptibility measurements were carried out using a SQUID Quantum Design MPMS magnetometer. An applied field of 1000 Oe was used. Afterward, zero-field-cooled (ZFC) and field-cooled (FC) measurements were conducted in the temperature range of 2−300 K. The data correction was done by removing the contribution from the sample holder.

2.4. Electrochemical Characterization of the Electrocatalyst. Catalytic ink was prepared by sonicating the mixture of the active material ZCP and Super P in a ratio of 3:1 in a solution of 250 μL of isopropyl alcohol and 750 μL of DI water for 5 min. It was followed by the addition of 20 μL of Nafion (binder) solution and further sonication for 1 h. An optimized amount of ink was drop cast on a clean, glassy carbon electrode of 4 mm diameter and then dried under an infrared lamp for 20−30 min. The electrocatalytic activity (ORR and OER) was measured using 0.1 M KOH as an electrolyte. Further, a three-electrode assembly was fabricated consisting of a calibrated saturated Hg/HgO reference electrode (details in Supporting Information), graphitic carbon rod counter electrode, and catalyst drop cast on a rotating ring disk electrode (RRDE) acting as a working electrode. Linear sweep voltammetry (LSV) experiments were performed at a constant voltage scan rate of 10 mV/s. Chronoamperometric (*i*−*t* curve) measurements were carried out at constant potentials close to their respective half-wave potentials. The data were converted to the reversible hydrogen electrode (RHE). All electrochemical tests were conducted with a CH instrument 7001E electrochemical workstation. The number of electrons (n) involved in the ORR was calculated using the Koutecky−Levich equation (K−L) as detailed in the Supporting Information.

2.5. Post-Mortem Analysis. Post-mortem studies were conducted using the sample collected after 100 cycles of electrocatalysis from the Toray carbon paper. The ex situ X-ray diffraction patterns (post ORR and OER) were acquired using a PANalytical X'pert pro diffractometer (Cu Kα source, λ_1 = 1.5405 Å, λ_2 = 1.5443 Å, operating at 40 kV/30 mA) in Bragg−Brentano geometry in the 2θ range of 15−70° (step size of 0.0262° s^{-1}). Oxidation states of Zn and Co in ex situ samples (post OER and ORR) were probed using X-ray photoelectron spectroscopy (XPS) by employing a monochromator X-ray beam of Al target having Kα radiation (ν = 1486.7 eV) accelerated at 12 kV and 6 mA. The shift was calibrated by taking a carbon signal with binding energy 284.6 eV as a reference. The

Table 1. Structural Refinement Results, Atomic Coordinates, and Isotropic Displacement Parameter Values for the Monoclinic $ZnCo_2(PO_4)_2$ Compound

source	synchrotron
wavelength	1.03319 Å
chemical formula	$ZnCo_2(PO_4)_2$
formula weight	373.20
temperature	ambient
pressure (if not ambient)	ambient
wavelength for constant wavelength or TOF	
crystal system	monoclinic
space group (no.)	$P2_1/n$ (#14)
$a, b, c, \alpha, \beta, \gamma$	a = 7.5435(1) Å, b = 8.3801(1) Å, c = 5.0538(1) Å, β = 94.375(1)°
V (Å^3)	318.553(3)
Z	2
d-space range (Å)	5.59756−0.96256
χ^2	81.043
R_p	7.56%
R_{wp}	9.98%
definition of R factors	R_p: residual of least-squares and R_{wp}: weighted residual

atom	site	x	y	z	occupancy	U_{iso} (Å^2)	site	sym.
Zn	Zn1	0.6163(18)	0.1397(15)	0.0880(26)	0.500	0.004(27)	4e	1
Co	Co1	0.6163(18)	0.1397(15)	0.0880(26)	0.500	0.056(7)	4e	1
Co	Co2	0.00000	0.00000	0.5000	1.000	0.018(11)	2b	−1
P	P1	0.1967(4)	0.1938(30)	0.0370(5)	1.000	0.018(12)	4e	1
O	O1	0.0536(7)	0.1416(7)	0.8216(11)	1.000	0.031(20)	4e	1
O	O2	0.1275(9)	0.1964(7)	0.3121(11)	1.000	0.032(20)	4e	1
O	O3	0.2545(7)	0.3616(7)	0.9441(10)	1.000	0.023(21)	4e	1
O	O4	0.3594(7)	0.0787(5)	0.0460(10)	1.000	0.015(19)	4e	1

background was fitted with Shirley's background function. The (micro)structure was analyzed using a transmission electron microscope (FEI Tecnai ST20, operated at 200 kV). Raman spectra were collected using a Horiba Jobin Yvon HR-Raman-123 MicroPL spectrometer with a green laser excitation source (λ = 519 nm). Fourier transform infrared (FTIR) spectra were acquired using a PerkinElmer Spectrum 100 Series FTIR spectrometer in the wavelength range of 400−4000 cm^{-1} (cycle number = 40). The samples were diluted with crystalline KBr and pressed into pellets to record the spectra.

2.6. Density Functional Theory (DFT) Calculations. First-principle electronic structure calculations were performed based on density functional theory (DFT) using the Vienna Ab initio simulation package (VASP) software.[34−37] The projector-augmented-wave (PAW) formalism[38] was implemented to determine the interaction between valence electrons and ions. The exchange−correlation interactions functional used in our calculations was based on the generalized gradient approximation (GGA) along with the Perdew−Burke−Ernzerhof (PBE)[39] to obtain the optimized structures of $ZnCo_2(PO_4)_2$, where the converged energy cutoff was chosen to be 500 eV. An adequate vacuum has been added to avoid periodicity and to create the surface. Further, the Brillouin zone was set using a 5 × 5 × 1 Monkhorst−Pack scheme for the ionic relaxation and to obtain the minimum energy configuration of the system. The self-consistency has been achieved with 10^{-4} eV energy convergence, and the structures were optimized until the Hellmann−Feynman forces were smaller than 10^{-3} eV/Å.[40] It is well known that the standard DFT and semi-local approximation for the exchange−correlation could not apprehend the dispersive forces, and thus a nonlocal correction term to describe the dispersive forces, e.g., DFT-D3 correction method of van der Waals dispersion, was used.[41] The projected density of states (PDOS) for this system was calculated to analyze the elemental orbital contribution of the constituent atoms in the valence and conduction band regime. Further, the OER and ORR activities of the system were determined by adsorbing O*, OH*, and OOH* (the asterisk denotes the adsorption site) atoms on the surface, and hence determining the free energy change of the reaction intermediates.

3. RESULTS AND DISCUSSION

3.1. Crystal Structure. The zinc-substituted cobalt phosphate (ZCP) was synthesized *via* a simple, fast, scalable solution combustion synthesis as described in detail in an earlier report.[42] Thermogravimetric analysis of the precursor mixture hinted at (i) complete material formation after 500 °C and (ii) stability of the resulting product till 800 °C (Figure S1). Thus, the synthesis was conducted between 600 and 800 °C for 6 h. Comparative XRD patterns (Figure S2) showed upon calcination at lower temperature (600 °C), while the target product forms, higher calcination temperature (800 °C) led to enhanced degree of crystallinity suitable for structural analysis. Even higher calcination temperature (T > 800 °C) led to decomposition and melting of the product material. So, the calcination temperature was fixed at 800 °C. The calcination duration was also optimized to 6 h, with longer calcination duration leading to better degree of crystallinity. To the best of our study, the crystal structure of ZCP is not yet solved till date. To gauge the phase purity and unveil the exact crystal structure of ZCP, synchrotron X-ray diffraction (SXRD) (at SLRI, Thailand) was employed. Rietveld refinement was performed using GSAS-II, where satisfactory refinement parameters were obtained. The resulting detailed structural information is provided in Tables 1, 2, and S1. ZCP was found to crystallize into an isotypic $Co_3(PO_4)_2$ type structure[43] consisting of a three-dimensional monoclinic framework with a $P2_1/n$ symmetry (Figure 1a). The structure was refined by replacing one Co site with Zn and varying the occupancy of Zn and Co while keeping the constraint of total occupancy to one. The monoclinic ZCP phase has the following lattice

Table 2. Polyhedral Bond Lengths and Bond Angles for CoO_6, CoO_5, ZnO_5, and PO_4 Polyhedra for the $ZnCo_2(PO_4)_2$ Compound[a]

(i) interatomic distance (Å)				(i) interatomic distance (Å)		(i) interatomic distance (Å)	
Co(1)−O(1)	2.249(6)	Co(2)−O(1)$^{\mathrm{iii}}$	2.028(6)	Zn(1)−O(1)	2.249(6)	P(1)−O(1)	1.537(6)
Co(1)−O(2)	1.963(6)	Co(2)−O(1)$^{\mathrm{iv}}$	2.028(6)	Zn(1)−O(2)	1.963(6)	P(1)−O(2)	1.522(7)
Co(1)−O(3)	2.010(6)	Co(2)−O(2)$^{\mathrm{iv}}$	2.162(7)	Zn(1)−O(3)	2.010(6)	P(1)−O(3)	1.555(7)
Co(1)−O(4)$^{\mathrm{I}}$	2.000(6)	Co(2)−O(2)$^{\mathrm{iii}}$	2.162(7)	Zn(1)−O(4)$^{\mathrm{I}}$	2.000(6)	P(1)−O(4)	1.559(6)
Co(1)−O(4)$^{\mathrm{ii}}$	1.965(5)	Co(2)−O(3)$^{\mathrm{i}}$	2.185(6)	Zn(1)−O(4)$^{\mathrm{ii}}$	1.965(5)	P(1)−O(1)	1.537(6)
		Co(2)−O(3)$^{\mathrm{ii}}$	2.185(6)				
Co(1) polyhedron		Co(2) polyhedron		Zn(1) polyhedron		P(1) polyhedron	
O(3)−O(1)	2.436(8)	O(1)−O(3)$^{\mathrm{i}}$	2.842(8)	O(3)−O(1)	2.436(8)	O(1)−O(3)	2.436(8)
O(3)−O(2)	3.545(8)	O(1)−O(3)$^{\mathrm{ii}}$	3.115(9)	O(3)−O(2)	3.545(8)	O(1)−O(2)	2.541(8)
O(3)−O(4)$^{\mathrm{iii}}$	3.140(8)	O(1)−O(2)$^{\mathrm{iii}}$	3.195(9)	O(3)−O(4)$^{\mathrm{iii}}$	3.140(8)	O(1)−O(4)	2.547(8)
O(3)−O(4)$^{\mathrm{iv}}$	3.502(8)	O(1)−O(2)$^{\mathrm{iv}}$	2.715(9)	O(3)−O(4)$^{\mathrm{iv}}$	3.502(8)	O(2)−O(4)	2.490(9)
O(1)−O(4)$^{\mathrm{iii}}$	4.182(8)	O(3)−O(2)$^{\mathrm{iii}}$	2.981(9)	O(1)−O(4)$^{\mathrm{iii}}$	4.182(8)	O(2)−O(3)	2.562(9)
O(1)−O(4)$^{\mathrm{iv}}$	3.044(8)	O(3)−O(2)$^{\mathrm{iv}}$	3.165(9)	O(1)−O(4)$^{\mathrm{iv}}$	3.044(8)	O(4)−O(3)	2.540(8)
O(2)−O(4)$^{\mathrm{iii}}$	3.283(8)	O(3)−O(3)	4.370(11)	O(2)−O(4)$^{\mathrm{iii}}$	3.283(8)		
O(2)−O(4)$^{\mathrm{iv}}$	3.067(9)	O(2)−O(2)	4.324(13)	O(2)−O(4)$^{\mathrm{iv}}$	3.067(9)		
O(4)−O(4)	2.570(11)	O(1)−O(1)	4.056(12)	O(4)−O(4)	2.570(11)		
O(2)−O(1)	2.715(9)			O(2)−O(1)	2.715(9)		
(ii) angles (deg)				(ii) angles (deg)		(ii) angles (deg)	
Co(1) polyhedron		Co(2) polyhedron		Zn(1) polyhedron		Zn(1) polyhedron	
O(3)−Co(1)−O(1)$^{\mathrm{i}}$	69.5(3)	O(1)−Co(2)−O(3)$^{\mathrm{i}}$	84.7(3)	O(3)−Zn(1)−O(1)$^{\mathrm{I}}$	69.5(3)	O(1)−P(1)−O(3)	104.0(4)
O(3)−Co(1)−O(2)$^{\mathrm{i}}$	126.3(3)	O(1)−Co(2)−O(3)$^{\mathrm{ii}}$	95.3(3)	O(3)−Zn(1)−O(2)$^{\mathrm{I}}$	126.3(3)	O(1)−P(1)−O(2)	112.3(4)
O(3)−Co(1)−O(4)$^{\mathrm{iii}}$	104.3(3)	O(1)−Co(2)−O(2)$^{\mathrm{iii}}$	99.3(3)	O(3)−Zn(1)−O(4)$^{\mathrm{iii}}$	104.3(3)	O(1)−P(1)−O(4)	110.7(4)
O(3)−Co(1)−O(4)$^{\mathrm{iv}}$	121.7(3)	O(1)−Co(2)−O(2)$^{\mathrm{iv}}$	80.7(3)	O(3)−Zn(1)−O(4)$^{\mathrm{iv}}$	121.7(3)	O(2)−P(1)−O(4)	107.8(4)
O(1)−Co(1)−O(4)$^{\mathrm{iii}}$	165.6(3)	O(3)−Co(2)−O(2)$^{\mathrm{iii}}$	86.6(3)	O(1)−Zn(1)−O(4)$^{\mathrm{iii}}$	165.6(3)	O(2)−P(1)−O(3)	112.7(4)
O(1)−Co(1)−O(4)$^{\mathrm{iv}}$	91.3(2)	O(3)−Co(2)−O(2)$^{\mathrm{iv}}$	93.4(3)	O(1)−Zn(1)−O(4)$^{\mathrm{iv}}$	91.3(2)	O(4)−P(1)−O(3)	109.3(4)
O(2)−Co(1)−O(4)$^{\mathrm{iii}}$	113.4(3)	O(3)−Co(2)−O(3)	180(0)	O(2)−Zn(1)−O(4)$^{\mathrm{iii}}$	113.4(3)		
O(2)−Co(1)−O(4)$^{\mathrm{iv}}$	101.4(3)	O(2)−Co(2)−O(2)	180(0)	O(2)−Zn(1)−O(4)$^{\mathrm{iv}}$	101.4(3)		
O(4)−Co(1)−O(4)	80.8(3)	O(1)−Co(2)−O(1)	180(0)	O(4)−Zn(1)−O(4)	80.8(3)		
O(2)−Co(1)−O(1)	79.9(3)			O(2)−Zn(1)−O(1)	79.9(3)		

[a] Symmetry operations: (i) $x + 1/2, -y + 1/2, z + 1/2$; (ii) $-x + 1/2, y + 1/2, -z + 1/2$; (iii) $-x, -y, -z$; (iv) x, y, z.

parameters: $a = 7.5435(1)$ Å, $b = 8.3801(1)$ Å, $c = 5.0538(1)$ Å, and $\beta = 94.375(1)°$ (similar to the PDF of the $Co_3(PO_4)_2$ compound: 01-070-2080). ZCP unit cell possesses one six-coordinated Co site and two five-coordinated Co sites. While Co^{2+} fully occupies the six-coordinated site, the five-coordinated sites are shared between Co^{2+} and Zn^{2+}.[30] The structure is built from an M_2O_8 (M = Co/Zn) unit formed by edge-sharing between two CoO_5/ZnO_5 distorted trigonal bipyramids. These M_2O_8 (M = Co/Zn) units are interconnected by bridging PO_4 tetrahedra and CoO_6 octahedra, in both corner-sharing and edge-sharing fashion, forming a three-dimensional framework (Figure 1b). The coordination around CoO_6 octahedra is illustrated in Figure 1a (inset) showing the (i) distorted trigonal bipyramid connectivity having both edge-sharing and corner-sharing, and (ii) CoO_6 bridged to the PO_4 units via corner-sharing. Along direction *a*, it forms a long chain comprising all of these polyhedra showing Zn and Co occupancy to be 0.5:0.5 (Figure 1b bottom).

The substitution of Zn^{2+} into the Co^{2+} position triggers shrinkage in the *a* and *c* axes, accompanied by expansion along the *b* axis, leading to an overall volume shrinkage of the ZCP unit cell (Figure S3). Further, the morphology of the pristine ZCP material was examined using both scanning and transmission electron microscopy (SEM/TEM). A porous morphology with nanometric uneven polygons (Figure 1c inset) having secondary particles in a size range 100−300 nm (Figure 1d) was observed. High-resolution transmission electron micrograph (HRTEM) depicted the high crystallinity in ZCP, and the lattice fringes were indexed to the (010) plane (Figure 1e) having *d* spacing of 0.830 nm. The selected area electron diffraction (SAED) data along the [001] zone axis revealed large single-crystalline domains of ZCP (Figure 1f). Further, elemental distribution mapping with STEM-EDS (energy dispersive X-ray spectroscopy) confirmed the uniform distribution of all constituting elements (Zn, Co, P, O) (Figures 1g and S4).

3.2. Magnetic Properties. Transition metal-based phosphates can exhibit interesting magnetic properties because of their structural diversity and rich crystal chemistry. The magnetic susceptibility (χ) of ZCP was examined in the temperature window of 2−300 K at 1000 Oe applied magnetic field in both FC and ZFC modes. As shown in Figure 2a, an antiferromagnetic (AFM) ordering was observed at Néel temperature T_N ~17.8 K. The inverse magnetic susceptibility (χ^{-1}) could be fitted linearly in the paramagnetic window (100−300 K) following the Curie−Weiss law $\chi = C/(T - \theta_{CW})$. It led to a Curie constant value of $C = 6.2936$ emu K mol^{-1}. The experimental μ_{eff} was computed to be 7.95 μ_B using the Curie constant ($\mu_{\mathrm{eff}} = \sqrt{8 \times c}$), which is closer to the μ_{eff} value of 5.196 μ_B per formula unit estimated based on the formulae: $\mu_{\mathrm{eff}} = (4S(S + 1) + L(L + 1))^{1/2}$ for the case of crystal field splitting of d-orbitals in a coordinated environment along with decoupled orbital angular momentum and spin angular momentum. At 2 K, the magnetization curve (M vs H)

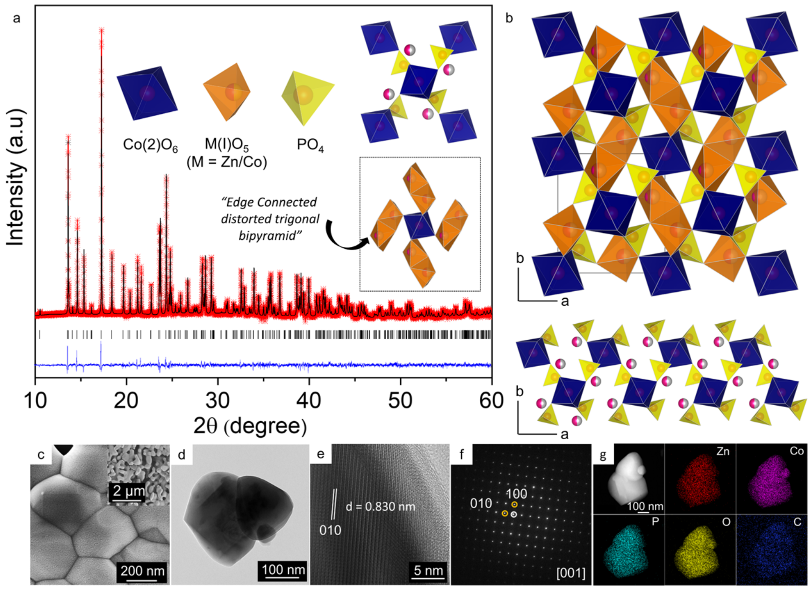

Figure 1. (a) Rietveld refined synchrotron (λ = 1.03319 Å) X-ray diffraction pattern of $ZnCo_2(PO_4)_2$ prepared at 800 °C for 6 h. The experimental data (red stars), calculated diffraction pattern (black line), and the Bragg diffraction positions (black ticks) are shown. Inset: Left − Co(2)O_6 octahedra (blue), M(Co/Zn)O_5 distorted trigonal bipyramid (orange), and PO_4 tetrahedra (yellow). Top right − Co(2)O_6 connectivity with PO_4 units (yellow) along with the M(Co/Zn)O_5 atom shown in pink and gray (0.5:0.5 occupancy of Zn/Co). Bottom right − Co(2)O_6 connectivity with two edge-shared M(Co/Zn)O_5 distorted trigonal bipyramids (orange). (b) Top: Crystal structure of $ZnCo_2(PO_4)_2$ assuming a monoclinic framework. Bottom: Long chains of Co(2)O_6 and M(Co/ZnO_5) polyhedra along *a* direction. (c) Morphology of $ZnCo_2(PO_4)_2$ shows uneven polygons and porous type morphology (inset). (d) Transmission electron microscopic image. (e, f) HRTEM micrograph and SAED pattern along the [001] zone axis confirms the crystalline nature of ZCP. (g) Elemental distribution maps showing homogeneous distribution of Zn (red), Co (purple), P (green), O (yellow), and C (blue).

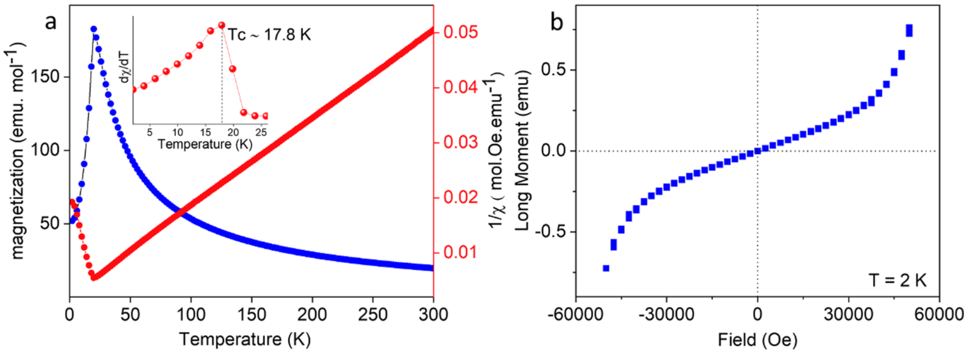

Figure 2. (a) Temperature-dependent magnetization curve of $ZnCo_2(PO_4)_2$ acquired in both zero-field-cooled (ZFC, blue dots) and field-cooled (FC, black line) modes at 1000 Oe in the temperature range of 2−300 K. The respective inverse magnetic susceptibility (red dots and line) vs temperature graph shows an inflection at 17.8 K due to antiferromagnetic transition (shown in inset). Curie−Weiss behavior was obtained after linear fitting of the paramagnetic window corresponding to the temperature range 100−300 K (red dashed line). (b) Magnetization (*M* vs *H*) graph of $ZnCo_2(PO_4)_2$ acquired at 2 K reveals the absence of any ferromagnetic hysteresis.

does not involve any hysteresis behavior indicative of the absence of any ferromagnetic contribution and/or existence of secondary impurity phases (Figure 2b). We are in the process of solving the antiferromagnetic structure of ZCP using low-temperature neutron powder diffraction, which will be described in a future communication.

3.3. Electrocatalytic Performance. Oxygen reduction reaction (ORR) was tested with a three-electrode setup with calibrated Hg/HgO (1 M NaOH) acting as the reference electrode (Figure S5), a carbon rod working as the counter electrode, and RRDE coated with a slurry of the optimized active electrocatalyst as the working electrode (Figure S6). The active material loading was ∼0.3 mg·cm^{-2}. The oxygen saturated 0.1 M KOH electrolyte was employed for the ORR study. Cyclic voltammogram (CV) for Pt/C and ZCP active materials was acquired in a 0.1 to −0.7 V (vs Hg/HgO) potential range (1 M NaOH), which was further converted to RHE (Figure S7). From these CV graphs, the ZCP onset potential was on the higher positive side (vs RHE). Linear sweep voltammetry (LSV) was performed at different rotations per minute (400−2025 rpm) (scan rate = 10 mV s^{-1}) (Figure 3a) to measure all of the ORR parameters. The current density (*j*) increased with higher rotation rates because of the availability of higher mass transport of oxygen on the electrode surface. The ORR data were compared with the benchmarked 20% Pt/C electrocatalyst. LSV of ZCP exhibited the exchange current density of 6.38 mA/cm^2 with a half-wave potential of 0.73 V and an onset potential of 0.87 V. While the half-wave potential and onset potential of ZCP are slightly less than the corresponding values of 0.85 and 1.01 V for the Pt/C

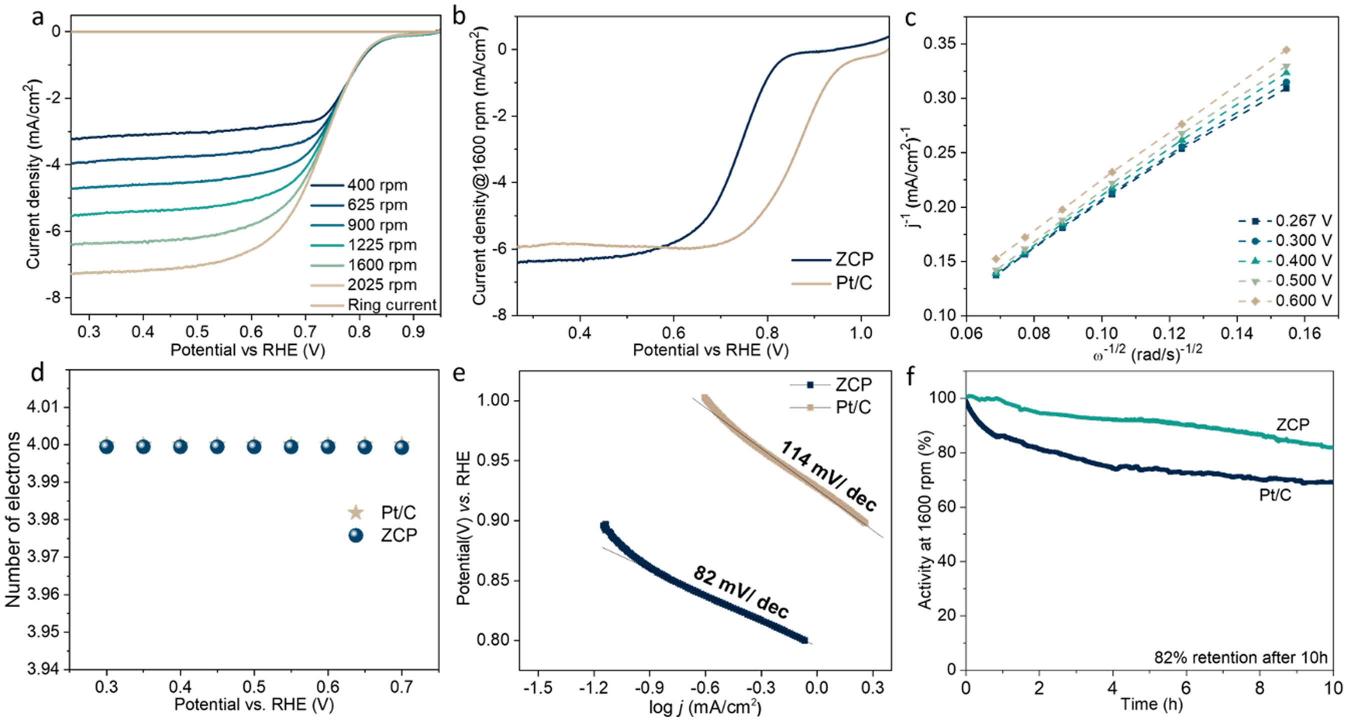

Figure 3. Oxygen reduction reaction activity of $ZnCo_2(PO_4)_2$. (a) Linear sweep voltammetry (LSV) at different rotation (400−2025 rpm) rates for 7.5 μL loading. (b) Comparison of ORR saturation current density of standard 20% Pt/C and $ZnCo_2(PO_4)_2$ at 1600 rpm. (c, d) Koutecky−Levich (K−L) graphs at various potentials showing near four-electron process in the reaction mechanism. (e) Tafel plot of $ZnCo_2(PO_4)_2$ during ORR analysis at 1600 rpm shows a value of 82 mV/dec. (f) Chronoamperometry stability test done for 10 h at constant potential.

benchmark, it exhibited the saturation current density similar to that of the Pt/C catalyst, which showed 5.98 mA/cm^2 at 1600 rpm (Figure 3b).

Various kinetic parameters were examined using the Koutecky−Levich (K−L) equation. The occurrence of linear and parallel lines in the K−L plot confirmed a first-order rate kinetics in ZCP (Figure 3c). To gauge the reaction pathway, it is essential to calculate the number of electron transfer involved in the actual reaction. ZCP showed close to 4 electron transfer during the reaction (Figure 3d). The Tafel slope of ZCP was superior to 20% Pt/C (Figure 3e), which indicates that the rate determining step (RDS) involved in the reaction has a value comparable to the theoretically derived slopes for Pt/C and it is ensuring a faster kinetics with lower overpotential of ZCP. ZCP was tested for operational stability using a chronoamperometry test for 10 h at 0.7 V. ZCP retained 82% of the original value post 10 h in comparison to Pt/C retaining only 69% of its original value (Figure 3f). Overall, ZCP worked as a stable ORR catalyst with activity comparable to the precious metal catalyst.

As oxygen evolution reaction (OER) is equally significant in metal−air batteries, the OER activity of $ZnCo_2(PO_4)_2$ was also studied in basic media (0.1 M KOH electrolyte). Suites of Co-based oxides and phosphates are well known to exhibit water-splitting properties.[15,16,19−22,44] The LSV results at 1600 rpm were compared with the standard RuO_2 catalyst. ZCP exhibited an onset potential of 1.50 V, and the saturation current was found to be 16.7 mA/cm^2. Both the onset potential and exchange current density were quite similar to the benchmark of the RuO_2 catalyst having an onset potential of 1.43 V and a saturation current value of 17.6 mA/cm^2 (Figure 4a). The OER exchange current density was stable up to 200 cycles, retaining ∼88% of the original saturation current density (Figure 4b). ZCP exhibited a comparable Tafel slope to that of RuO_2.

The efficient ORR and OER exchange current densities could be ascribed to the presence of a large number of Co active sites and a surface area of 3.241 m^2/g, measured by the Brunauer−Emmett−Teller (BET) method using N_2 gas adsorption (Figure S8). Also, the electrochemically active surface area (ECSA) was derived using the slope of double-layer capacitance (C_{dl} value) of 1/2 ($J_c - J_a$) (at 1.247 V) vs scan rate (Figure S9). The ECSA value was calculated to be 1.2160 cm^2. Overall, this enhanced catalytic activity of ZCP can stem from the presence of a large number of Co sites having asymmetric CoO_5/CoO_6 polyhedra (structural distortion coefficient given in Supporting Information) and edge-sharing formation, which can enhance bifunctional catalytic performance (Figure 4c). Owing to the presence of Zn in the system, it offers a large number of asymmetric edge-sharing polyhedra inducing distortion where water molecules preferably bind leading to enhanced bifunctional activity of the catalyst.[22] Also, the substitution of Zn could modify the Co−OH bond adsorption energy to get the most appropriate energy state and lower down the overpotential for OER reaction. Overall, the idea here is to incorporate ions (such as Zn) that allow the catalyst to have similar energy released due to the $M^{n+}-O_2^{2-}$ (M = Co) bond formation on the surface of the catalyst to the energy needed to break the $M^{n+}-OH^-$ bond. This ensures fast displacement of O^{2-}/OH^- and OH^- regeneration. This approach can be extended to other divalent ions which have a comparable size to Co.[45,46] Hence, ZCP offers an economic system exhibiting bifunctional electrocatalytic activity with low overpotential (0.95 eV) with operational stability. This electrocatalytic activity is comparable with many other non-noble electrocatalysts such as

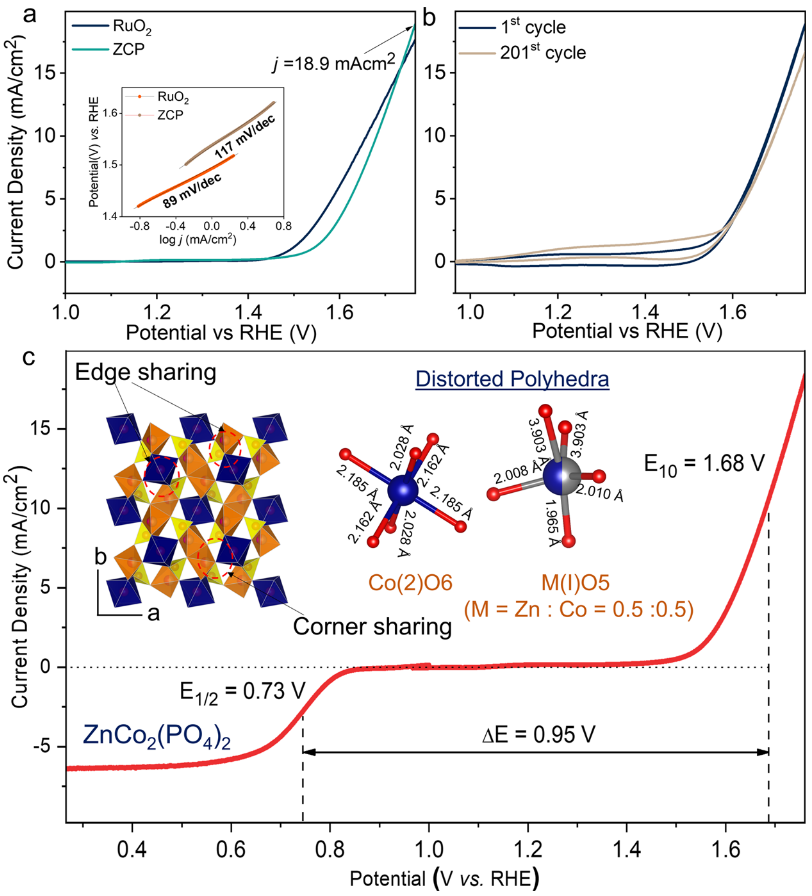

Figure 4. Oxygen evolution reaction for $ZnCo_2(PO_4)_2$. (a) OER LSV curves of $ZnCo_2(PO_4)_2$ in comparison to RuO_2. Inset: Tafel plot of ZCP and RuO_2. (b) Stability of $ZnCo_2(PO_4)_2$ for 200 cycles shows a slight change in the current density. (c) Bifunctional performance of ZCP: calculation of $\Delta E = (E_{\mathrm{ORR}\ =\ -3\ \mathrm{mA\ cm^{-2}}} - E_{\mathrm{OER}\ =\ 10\ \mathrm{mA\ cm^{-2}}})$, overpotential values for both ORR and OER reactions. Inset: (Left) Local coordination of polyhedra consisting of edge and corner sharing. (Right) Bond lengths of distorted polyhedral of Co and Zn atoms.

$Co_3(PO_4)_2$@NC,[20] $Mn_3(PO_4)_2$,[21] and Ni-based phosphates.[24] The detailed comparison with a few (non) oxide catalysts is presented in Tables S2−S5.

3.4. Theoretical Calculations.

The adsorption energies of the intermediate reactants construct the reaction coordinate that helps to understand the OER and ORR catalytic activities. In general, the OER activity in the acidic medium has four steps involving concerted proton−electron transfer on surface sites, which comprises three distinct adsorbing reaction intermediates such as OH*, O*, and OOH*.[47] Here, for the calculations, the system was considered to be at pH = 0. The reaction intermediate steps of the OER can be written as follows (a1−a4):

$$H_2O + {}^* \rightarrow OH^* + H^+ + e^- \tag{a1}$$

$$OH^* \rightarrow O^* + H^+ + e^- \tag{a2}$$

$$O^* + H_2O \rightarrow OOH^* + H^+ + e^- \tag{a3}$$

$$OOH^* \rightarrow O_2\ \uparrow + H^+ + e^- \tag{a4}$$

The adsorption free energy change (ΔG) of these reaction intermediates in each step was determined. The difference in free energy was employed as the descriptor of the OER activity of the electrocatalyst. The change in the free energy for the reaction intermediates can be derived by eqs b1 and b2.

$$\Delta G_1 = \Delta G_{O^*} - \Delta G_{OH^*} - eU + k_bT \ln \mathrm{pH}^+ \tag{b1}$$

$$\Delta G_2 = \Delta G_{OOH^*} - \Delta G_{O^*} - eU + k_bT \ln \mathrm{pH}^+ \tag{b2}$$

where $\Delta G_{1/2}$ is the Gibbs free energy change, pH^+ is the activity of the protons, the term eU comes from standard hydrogen electrode (SHE) potential, and ΔG_{O^*}, ΔG_{OH^*}, and ΔG_{OOH^*} are the Gibbs free energy of the adsorbed atoms O*, OH*, and OOH*, respectively. These values can be obtained from the adsorption energy where there is small additive correction added to the adsorption energy, which are 0.05, 0.35, and 0.40 eV for O, OH, and OOH, respectively.[48] Nørskov et al.[48,49] predicted that the adsorption free energy for each step varies similarly as pH and the potential value. Hence, the theoretical overpotential can be independent of these two parameters. In our calculation, we have calculated the free energy analysis in a standard condition (pH = 0 and U = 0). For different systems, the adsorption energies can be calculated using formula c

$$E_Y^{\mathrm{ads}} = E_T[\mathrm{system} + Y] - E_T[\mathrm{system}] - E_T[Y] \tag{c}$$

where E_T [system + Y] is the energy of $ZnCo_2(PO_4)_2$ along with the adsorbed atom, and E_T [system] is the energy, whereas E_T [Y] is the total energy for isolated OH and OOH molecules. In the case of O adsorbate, we have determined the O_2 molecule energy in the gas phase and corrected it after dividing by 2 in the third term. Various possible adsorption sites and orientation of molecules (OH and OOH) were checked, and the top of the Co atom was found as the most

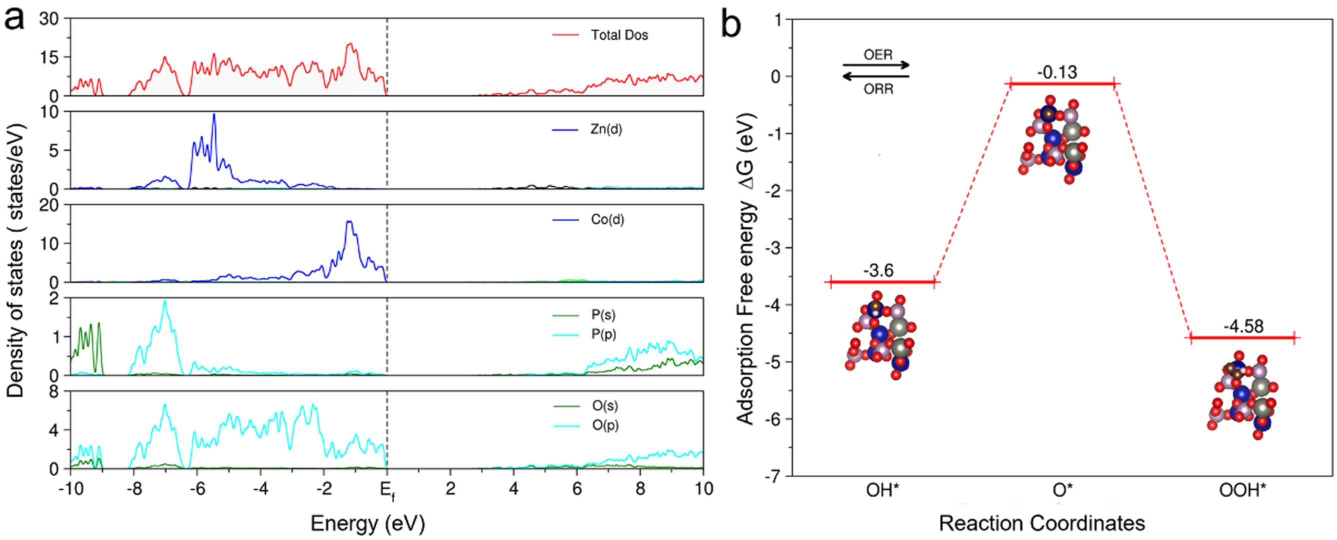

Figure 5. DFT analysis of ZCP: (a) projected density of states of ZCP visualizing the orbital contribution from each atom. (b) Adsorption coordinates of OER and ORR, respectively (brown color balls = adsorbed O, pink color ball = H, blue color balls = Co, and gray color balls = Zn).

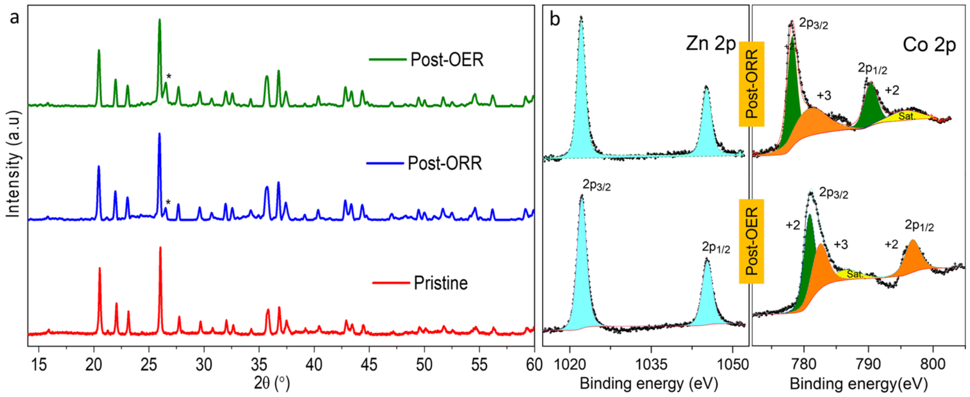

Figure 6. Ex situ structural analysis of $ZnCo_2(PO_4)_2$. (a) Ex situ X-ray diffraction patterns of OER and ORR samples. (b) Comparative XPS spectra showing no change in Zn (Zn $2p_{1/2}$ and Zn $2p_{3/2}$) and Co (Co $2p_{1/2}$ and Co $2p_{3/2}$) peaks post ORR and OER operation.

favorable site. Alongside this, the thermodynamic stability of ZCP has also been determined using eq d[50]

$$\Delta H_f = E_{ZCP} - \sum_i \mu_i n_i \tag{d}$$

where E_{ZCP} is the total energy of ZCP obtained using DFT calculation, and μ_i and n_i are the chemical potential and number of each atom present in ZCP (i.e., Zn, Co, P, and O). The formation energy calculated had a negative value (−1.24 eV/atom) which signifies that ZCP is thermodynamically stable.

Further, the electronic structure was analyzed using the projected density of state (PDOS) as shown in Figure 5a. The PDOS representation shows that $ZnCo_2(PO_4)_2$ has a wider band gap. Further, the orbital contribution exhibits the contribution of the outermost Co(d) and O(p) orbitals being dominant in the valence band region near the Fermi level, whereas in the conduction band region, the orbital contribution is solely due to the O(p) orbital. This gives lighter evidence that the transfer of electron holes in the OER and ORR processes is mainly from the Co atom, which was further proved true during the adsorption calculation, where the top of Co is the most favorable site. The oxygen evolution reaction adsorption coordinates are shown in Figure 5b. It was investigated that the reaction step from the OH* → O* formation is energetically favorable for half OER pathway, whereas the path step from the O* → OOH* formation is not found to be energetically favorable. Thus, the O* → OOH* step offers large hindrance.[49,51] The ORR intermediates are the same as OER intermediates (Figure 5b). If the electrocatalyst shows uphill behavior, it is a good sign of OER activity, whereas the downhill nature of the graph depicts the better performance for an ORR reaction. Hence, it is observed that the first half of the reaction, i.e., OOH* → O* is energetically unfavorable, while the second half of the reaction O* → OH* pathway is energetically favorable (Figure 5b).

3.5. Post-Mortem Analysis. While designing novel electrocatalysts, it is essential to ensure the structural and functional stability over long operation duration. The (de)-adsorption and surface bond formation/breakage can lead to structural degradation. The structural stability of ZCP was probed by XRD post-catalysis (after 100 cycles of ORR/OER). No evident structural change was observed except a shoulder peak of 26° peak (Figure 6a), which could have come from residual carbon (during electrode preparation). Subsequently, the chemical oxidation states of ZCP samples were probed using XPS post-electrocatalytic (ORR/OER) operation over 100 cycles. XPS also revealed no significant change in the oxidation states of constituent Zn and Co species (Figure 6b). The binding energies were comparable to the pristine Zn and Co species (Figure S10). The fitting parameters (FWHM, % area) are compiled in Table S6.

The local structural integrity was further probed by post-mortem TEM analysis of samples recovered after 100 cycles of ORR/OER operation. The post ORR/OER samples of ZCP showed slight amorphization and disintegration of particles (Figure 7a,d). However, crystalline domains were observed to be embedded in an amorphous matrix as shown in the HRTEM micrograph (Figure 7b,e) and the SAED pattern (Figure 7c,f) of post ORR/OER samples. The *d* spacing for the post-OER sample was 0.84 nm corresponding to the (010) plane. For the post-ORR sample, the *d* parameter was 0.365 nm and 0.395 nm for the (110) and (111) planes, respectively, closer to the pristine material. The Raman spectra showed D and G bands, whereas there was no change in the FTIR spectra after OER and ORR activities (Figure S11). Thus, it was confirmed that structural stability of the $ZnCo_2(PO_4)_2$ catalyst was retained post-electrocatalytic cycling with a high degree of crystallinity with a small number of disintegrated particles.

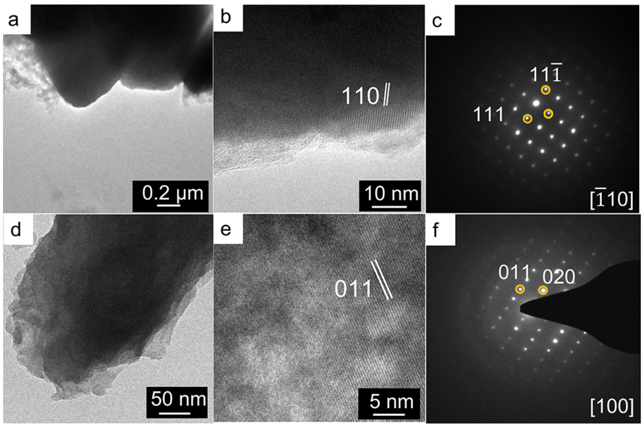

Figure 7. Ex situ TEM analysis showing structural integrity for post-ORR (a−c) and post-OER samples (d−f) taken after 100 cycles. (b) The (110) plane in the post-ORR sample corresponds to a *d* spacing of 0.365 nm. (c) The diffraction pattern corresponds to the zone axis [110]. (e) The (011) plane in ex situ OER sample shows a *d* spacing of 0.84 nm. (f) The diffraction pattern corresponds to the zone axis of [100].

4. CONCLUSIONS

In summary, a monoclinic three-dimensional framework zinc-substituted cobalt phosphate [$ZnCo_2(PO_4)_2$] has been demonstrated as a low-cost and efficient bifunctional electrocatalyst. The crystal structure of this monoclinic phosphate was solved with synchrotron X-ray diffraction. Prepared by scalable solution combustion synthesis, it has a porous morphology having uneven nanometric polygons. $ZnCo_2(PO_4)_2$ exhibited robust oxygen reduction and oxygen evolution (ORR and OER) reaction activities with onset potential values of 0.87 and 1.50 V (vs RHE), respectively. ORR saturated current density was 6.38 mA/cm^2, close to the benchmark of the 20% Pt/C catalyst. It also showed an OER exchange current density of 16.7 mA/cm^2, close to the state-of-the-art RuO_2 (j = 17.6 mA/cm^2) catalyst. The substitution of Zn cation into Co sites creates structural distortion on the interstitial site, which enhances the bifunctional electrocatalytic performance. Because of this asymmetry, it enabled the optimum bond strength of $Co^{2+}-O^{2-}$ for the faster kinetics of ORR and OER reactions. DFT calculations suggested that $ZnCo_2(PO_4)_2$ has a suitable binding energy toward O_2 as well as the oxygenated species O* and OH*. Also, the material is thermodynamically stable with a negative formation energy value. Hence, $ZnCo_2(PO_4)_2$ forms a new phosphate candidate for electrocatalysis having structural stability as evident from post-mortem analyses. Taking advantage of its bifunctional activity, it can be implemented in zinc−air batteries. This work further enriches the PO_4-based material database for development of economic electrocatalysts for rechargeable metal−air batteries.

AUTHOR INFORMATION

Corresponding Author

Prabeer Barpanda − *Faraday Materials Laboratory (FaMaL), Materials Research Centre, Indian Institute of Science, Bangalore 560012, India; Electrochemical Energy Storage, Helmholtz Institute Ulm (HIU), Ulm 89081, Germany; Institute of Nanotechnology, Karlsruhe Institute of Technology (KIT), Karlsruhe 76021, Germany;* orcid.org/0000-0003-0902-3690; Email: prabeer@iisc.ac.in

Authors

Deepa Singh − *Faraday Materials Laboratory (FaMaL), Materials Research Centre, Indian Institute of Science, Bangalore 560012, India*

Shashwat Singh − *Faraday Materials Laboratory (FaMaL), Materials Research Centre, Indian Institute of Science, Bangalore 560012, India*

Ponnappa Kechanda Prasanna − *Materials Theory for Energy Scavenging (MATES) Lab, Harish-Chandra Research Institute (HRI), A C.I. of Homi Bhabha National Institute (HBNI), Prayagraj 211019, India*

Rajeev Kumar Rai − *Materials Research Centre, Indian Institute of Science, Bangalore 560012, India;* orcid.org/0000-0002-2248-7601

Prae Chirawatkul − *Synchrotron Light Research Institute (SLRI), Nakhon Ratchasima 30000, Thailand*

Sudip Chakraborty − *Materials Theory for Energy Scavenging (MATES) Lab, Harish-Chandra Research Institute (HRI), A C.I. of Homi Bhabha National Institute (HBNI), Prayagraj 211019, India;* orcid.org/0000-0002-6765-2084

Maximilian Fichtner − *Electrochemical Energy Storage, Helmholtz Institute Ulm (HIU), Ulm 89081, Germany;*

Institute of Nanotechnology, Karlsruhe Institute of Technology (KIT), Karlsruhe 76021, Germany; orcid.org/0000-0002-7127-1823

Author Contributions

D.S. carried out most of the experiments and wrote the first draft. S.S. performed the magnetic analysis. P.K.P. performed the DFT-based electronic structure calculations under the supervision of S.C. R.K.R. performed the TEM analysis. P.C. conducted the synchrotron structure analysis at SLRI-Thailand. P.B. arranged the funding and directed this project. All authors were involved in data interpretation and preparation of the manuscript.

Notes

The authors declare no competing financial interest.

ACKNOWLEDGMENTS

The current project was financially supported by the Technology Mission Division (DST, Government of India) under the aegis of Materials for Energy Storage (MES-2018) program (DST/TMD/MES/2k18/00217). D.S. and S.S. thank the Ministry of Human Resource Development (MHRD, Government of India) for student fellowships. S.S. is grateful to LAFICS (Indian-French Laboratory of Solid State Chemistry) for exchange visit to France and Prof. Valérie Pralong for hosting him. D.S. acknowledges A. Baby, Prof. T. N. Guru Row, and Prof. Balaram Sahoo for scientific discussion. P.K.S. and S.C. are grateful to HRI and DST-SERB (SRG/2020/001707) for generous funding. Computational work was carried out at the cluster computing facility at HRI. R.K.R. acknowledges the Advanced Facility for Microscopy and Microanalysis (AFMM, IISC) for providing the TEM facility. P.B. is grateful to the Alexander von Humboldt Foundation (Bonn, Germany) for a 2022 Humboldt fellowship for experienced researchers.

REFERENCES

(1) Mallouk, T. E. Water Electrolysis: Divide and Conquer. *Nat. Chem.* **2013**, *5*, 362−363.

(2) Gür, T. M. Review of Electrical Energy Storage Technologies, Materials, and Systems: Challenges and Prospects for Large-Scale Grid Storage. *Energy Environ. Sci.* **2018**, *11*, 2696−2767.

(3) Suntivich, J.; May, K. J.; Gasteiger, H. A.; Goodenough, J. B.; Shao-Horn, Y. A Perovskite Oxide Optimized for Oxygen Evolution Catalysis from Molecular Orbital Principles. *Science* **2011**, *334*, 1383−1385.

(4) Turner, J. A. Sustainable Hydrogen Production. *Science* **2004**, *305*, 972−974.

(5) Yang, H.; Han, X.; Douka, A. I.; Huang, L.; Gong, L.; Xia, C.; Park, H. S.; Xia, B. Y. Advanced Oxygen Electrocatalysis in Energy Conversion and Storage. *Adv. Funct. Mater.* **2021**, *31*, No. 2007602.

(6) Zhang, J.; Zhao, Z.; Xia, Z.; Dai, L. A Metal-free Bifunctional Electrocatalyst for Oxygen Reduction and Oxygen Evolution Reactions. *Nat. Nanotechnol.* **2015**, *10*, 444−452.

(7) Li, Y.; Gong, M.; Liang, Y.; Feng, J.; Kim, J.-E.; Wang, H.; Hong, G.; Zhang, B.; Dai, H. Advanced Zinc-Air Batteries Based on High-Performance Hybrid Electrocatalysts. *Nat. Commun.* **2013**, *4*, No. 1805.

(8) Ge, X.; Sumboja, A.; Wuu, D.; An, T.; Li, B.; Goh, F. T.; Hor, T. A.; Zong, Y.; Liu, Z. Oxygen Reduction in Alkaline Media: From Mechanisms to Recent Advances of Catalysts. *ACS Catal.* **2015**, *5*, 4643−4667.

(9) Katsounaros, I.; Cherevko, S.; Zeradjanin, A. R.; Mayrhofer, K. J. J. Oxygen Electrochemistry as a Cornerstone for Sustainable Energy Conversion. *Angew. Chem., Int. Ed.* **2014**, *53*, 102−121.

(10) Abirami, M.; Hwang, S. M.; Yang, J.; Senthilkumar, S.; Kim, J.; Go, W.-S.; Senthilkumar, B.; Song, H.-K.; Kim, Y. A Metal-Organic Framework Derived Porous Cobalt Manganese Oxide Bifunctional Electrocatalyst for Hybrid Na-air/Seawater Batteries. *ACS Appl. Mater. Interfaces* **2016**, *8*, 32778−32787.

(11) Yan, Y.; Xia, B. Y.; Zhao, B.; Wang, X. A Review on Noble-Metal-Free Bifunctional Heterogeneous Catalysts for Overall Electrochemical Water Splitting. *J. Mater. Chem. A* **2016**, *4*, 17587−17603.

(12) Gordon, R. B.; Bertram, M.; Graedel, T. E. Metal Stocks and Sustainability. *Proc. Natl. Acad. Sci. U.S.A.* **2006**, *103*, 1209−1214.

(13) Kumar, Y.; Mooste, M.; Tammeveski, K. Recent Progress of Transition Metal-Based Bifunctional Electrocatalysts for Rechargeable Zinc−Air Battery Application. *Curr. Opin. Electrochem.* **2023**, *38*, No. 101229.

(14) Ren, S.; Duan, X.; Liang, S.; Zhang, M.; Zheng, H. Bifunctional electrocatalysts for Zn−air batteries: recent developments and future perspectives. *J. Mater. Chem. A* **2020**, *8*, 6144−6182.

(15) Maiyalagan, T.; Jarvis, K. A.; Therese, S.; Ferreira, P. J.; Manthiram, A. Spinel-type Lithium Cobalt Oxide as a Bifunctional Electrocatalyst for the Oxygen Evolution and Oxygen Reduction Reactions. *Nat. Commun.* **2014**, *5*, No. 3949.

(16) Lee, S. W.; Carlton, C.; Risch, M.; Surendranath, Y.; Chen, S.; Furutsuki, S.; Yamada, A.; Nocera, D. G.; Shao-Horn, Y. The Nature of Lithium Battery Materials Under Oxygen Evolution Reaction Conditions. *J. Am. Chem. Soc.* **2012**, *134*, 16959−16962.

(17) Sharma, L.; Gond, R.; Senthilkumar, B.; Roy, A.; Barpanda, P. Fluorophosphates as Efficient Bifunctional Electrocatalysts for Metal-Air Batteries. *ACS Catal.* **2020**, *10*, 43−50.

(18) Sada, K.; Gond, R.; Bothra, N.; Pati, S. K.; Barpanda, P. Potassium Cobalt Pyrophosphate as a Nonprecious Bifunctional Electrocatalyst for Zinc-Air Batteries. *ACS Appl. Mater. Interfaces* **2022**, *14*, 8992−9001.

(19) Gond, R.; Singh, D. K.; Eswaramoorthy, M.; Barpanda, P. Sodium Cobalt Metaphosphate as an Efficient Oxygen Evolution Reaction Catalyst in Alkaline Solution. *Angew. Chem., Int. Ed.* **2019**, *131*, 8418−8423.

(20) Yuan, C. Z.; Jiang, Y. F.; Wang, Z.; Xie, X.; Yang, Z. K.; Yousaf, A. B.; Xu, A. W. Cobalt Phosphate Nanoparticles Decorated with Nitrogen-Doped Carbon Layers as Highly Active and Stable Electrocatalysts for the Oxygen Evolution Reaction. *J. Mater. Chem. A* **2016**, *4*, 8155−8160.

(21) Gorlin, Y.; Jaramillo, T. F. A Bifunctional Nonprecious Metal Catalyst for Oxygen Reduction and Water Oxidation. *J. Am. Chem. Soc.* **2010**, *132*, 13612−13614.

(22) Kim, H.; Park, J.; Park, I.; Jin, K.; Jerng, S. E.; Kim, S. H.; Nam, K. T.; Kang, K. Coordination Tuning of Cobalt Phosphates Towards Efficient Water Oxidation Catalyst. *Nat. Commun.* **2015**, *6*, No. 8253.

(23) Guo, R.; Lai, X.; Huang, J.; Du, X.; Yan, Y.; Sun, Y.; Zou, G.; Xio, J. Phosphate-Based Electrocatalysts for Water Splitting: Recent Progress. *ChemElectroChem* **2018**, *5*, 3822−3834.

(24) Zhan, Y.; Lu, M.; Yang, S.; Liu, Z.; Lee, J. Y. The Origin of Catalytic Activity of Nickel Phosphate for Oxygen Evolution in Alkaline Solution and its Further Enhancement by Iron Substitution. *ChemElectroChem* **2016**, *3*, 615−621.

(25) Zhao, Q.; Yan, Z.; Chen, C.; Chen, J. Spinels: Controlled Preparation, Oxygen Reduction/Evolution Reaction Application, and Beyond. *Chem. Rev.* **2017**, *117*, 10121−10211.

(26) Wang, H.; Liu, R.; Li, Y.; Lu, X.; Wang, Q.; Zhao, S.; Yuan, K.; Cui, Z.; Li, X.; Xin, S.; Zhang, R.; Lei, M.; Lin, Z. Durable and Efficient Hollow Porous Oxide Spinel Microspheres for Oxygen Reduction. *Joule* **2018**, *2*, 337−348.

(27) Baby, A.; Senthilkumar, B.; Barpanda, P. Low-Cost Rapid Template-Free Synthesis of Nanoscale Zinc Spinels for Energy Storage and Electrocatalytic Applications. *ACS Appl. Energy Mater.* **2019**, *2*, 3211−3219.

(28) Nersisyan, H. H.; Lee, J. H.; Ding, J.-R.; Kim, K.-S.; Manukyan, K. V.; Mukasyan, A. S. Combustion Synthesis of Zero-, One-, Two- and Three-Dimensional Nanostructures: Current Trends and Future Perspectives. *Prog. Energy Combust. Sci.* **2017**, *63*, 79−118.

(29) Shannon, R. D. Revised Effective Ionic Radii and Systematic Studies of Interatomic Distances in Halides and Chalcogenides. *Acta Crystallogr., Sect. A* **1976**, *32*, 751−767.

(30) Nord, A. G. Crystallographic Studies of the Farringtonite-type Phases γ-$Zn_2Co(PO_4)_2$ and γ-$(Zn_{0.50}Co_{0.50})_3(PO_4)_2$. *Acta Crystallogr., Sect. B* **1984**, *40*, 191−194.

(31) Ling, T.; Yan, D. Y.; Jiao, Y.; Wang, H.; Zheng, Y.; Zheng, X.; Mao, J.; Du, X. W.; Hu, Z.; Jaroniec, M.; Qiao, S. Z. Engineering Surface Atomic Structure of Single-Crystal Cobalt (II) Oxide Nanorods for Superior Electrocatalysis. *Nat. Commun.* **2016**, *7*, No. 12876.

(32) Toby, B. H.; Von Dreele, R. B. GSAS-II: The Genesis of a Modern Open-Source All-Purpose Crystallography Software Package. *J. Appl. Crystallogr.* **2013**, *46*, 544−549.

(33) Momma, K.; Izumi, F. VESTA 3 for Three-Dimensional Visualization of Crystal, Volumetric and Morphology Data. *J. Appl. Crystallogr.* **2011**, *44*, 1272−1276.

(34) Hohenberg, P.; Kohn, W. Inhomogeneous Electron Gas. *Phys. Rev.* **1964**, *136*, B864.

(35) Kohn, W.; Sham, L. J. Self-consistent Equations Including Exchange, and Correlation Effects. *Phys. Rev.* **1965**, *140*, A1133.

(36) Kresse, G.; Furthmüller, J. Efficient Iterative Schemes for Ab Initio Total-energy Calculations Using a Plane-wave Basis Set. *Phys. Rev. B* **1996**, *54*, 11169−11186.

(37) Kresse, G.; Furthmüller, J. Efficiency of Ab-initio Total Energy Calculations for Metals and Semiconductors Using a Plane-wave Basis Set. *Comput. Mater. Sci.* **1996**, *6*, 15−50.

(38) Blöchl, P. E. Projector Augmented-Wave Method. *Phys. Rev. B* **1994**, *50*, 17953−17979.

(39) Perdew, J. P.; Burke, K.; Ernzerhof, M. Generalized Gradient Approximation Made Simple. *Phys. Rev. Lett.* **1996**, *77*, 3865−3868.

(40) Monkhorst, H. J.; Pack, J. D. Special Points for Brillouin-Zone Integrations. *Phys. Rev. B* **1976**, *13*, 5188−5192.

(41) Nørskov, J. K.; Rossmeisl, J.; Logadottir, A.; Lindqvist, L.; Kitchin, J. R.; Bligaard, T.; Jonsson, H. Origin of the Overpotential for Oxygen Reduction at a Fuel-Cell Cathode. *J. Phys. Chem. B* **2004**, *108*, 17886−17892.

(42) Baby, A.; Singh, D.; Murugesan, C.; Barpanda, P. The Design of Zinc-substituted Cobalt (Pyro) Phosphates as Efficient Bifunctional Electrocatalysts for Zinc−air Batteries. *Chem. Commun.* **2020**, *56*, 8400−8403.

(43) Anderson, J.; Kostiner, E.; Miller, M.; Rea, J. R. The Crystal Structure of Cobalt Orthophosphate $Co_3(PO_4)_2$. *J. Solid State Chem.* **1975**, *14*, 372−377.

(44) Zhan, Y.; Lu, M.; Yang, S.; Xu, C.; Liu, Z.; Lee, J. Y. Activity of Transition-Metal (Manganese, Iron, Cobalt, and Nickel) Phosphates for Oxygen Electrocatalysis in Alkaline Solution. *ChemCatChem* **2016**, *8*, 372−379.

(45) Wang, H.; Liu, R.; Li, Y.; Zhang, R.; Lei, M.; Lin, Z.; et al. Durable and Efficient Hollow Porous Oxide Spinel Microspheres for Oxygen Reduction. *Joule* **2018**, *2*, 337−348.

(46) Stephens, I. E. L.; Bondarenko, A. S.; Grønbjerg, U.; Rossmeislc, J.; Chorkendorff, I. Understanding the Electrocatalysis of Oxygen Reduction on Platinum and its Alloys. *Energy Environ. Sci.* **2012**, *5*, 6744−6762.

(47) Rossmeisl, J.; Qu, Z.-W.; Zhu, H.; Kroes, G.-J.; Nørskov, J. K. Electrolysis of Water on Oxide Surfaces. *J. Electroanal. Chem.* **2007**, *607*, 83−89.

(48) Man, I. C.; Su, H. Y.; Calle-Vallejo, F.; Hansen, H. A.; Martínez, J. I.; Inoglu, N. G.; Kitchin, J.; Jaramillo, T. F.; Nørskov, J. K.; Rossmeisl, J. Universality in Oxygen Evolution Electrocatalysis on Oxide Surfaces. *ChemCatChem* **2011**, *3*, 1159−1165.

(49) Garlyyev, B.; Fichtner, J.; Piqué, O.; Schneider, O.; Bandarenka, A. S.; Bandarenka, A. S.; Calle-Vallejo, F. Revealing the Nature of Active Sites in Electrocatalysis. *Chem. Sci.* **2019**, *10*, 8060−8075.

(50) Bahamon, D.; Khalil, M.; Belabbes, A.; Alwahedi, Y.; Vega, L. F.; Polychronopoulou, K. A. DFT Study of the Adsorption Energy and Electronic Interactions of the SO2 Molecule on a Cop Hydrotreating Catalyst. *RSC Adv.* **2021**, *11*, 2947−2957.

(51) Kirklin, S.; Saal, J. E.; Meredig, B.; Thompson, A.; Doak, W. J.; Aykol, M.; Rühl, S.; Wolverton, C. The Open Quantum Materials Database (OQMD): assessing the accuracy of DFT formation energies. *npj Comput. Mater.* **2015**, *1*, 15010.